Available online at www.sciencedirect.com

ScienceDirect

Advances in Space Research 74 (2024) 271–283

ADVANCES IN SPACE RESEARCH (a COSPAR publication)

www.elsevier.com/locate/asr

Characteristics of ionospheric disturbances during the 2021 Typhoon Chanthu based on GPS and GLONASS

Mengwei Ma [a], Shuanggen Jin [a,b,c,*], Xuzhan T. Jin [d]

[a] School of Remote Sensing and Geomatics Engineering, Nanjing University of Information Science and Technology, Nanjing 210044, China
[b] School of Surveying and Land Information Engineering, Henan Polytechnic University, Jiaozuo 454003, China
[c] Shanghai Astronomical Observatory, Chinese Academy of Sciences, Shanghai 200030, China
[d] College of Information Science and Engineering, Henan University of Technology, Zhengzhou 450001, China

Received 24 October 2023; received in revised form 20 March 2024; accepted 25 March 2024
Available online 28 March 2024

Abstract

Severe typhoons often result in substantial economic and human losses. Therefore, near-real-time monitoring and forecasting of severe typhoons have a significant importance. In this paper, characteristics of ionospheric disturbances during the 2021 Typhoon Chanthu are estimated and investigated from GPS and GLONASS measurements. We calculate high-precision de-trended and filtered ionospheric vertical total electron content (VTEC) data based on GPS and GLONASS data from intensive Global Navigation Satellite System (GNSS) observations at 30-second intervals in Taiwan. Based on the VTEC values, we analyze the characteristics of ionospheric disturbances caused by Typhoon Chanthu, such as the time of appearance of ionospheric disturbances, changes in the magnitude of these disturbances, alterations in two-dimensional disturbances, fluctuations in the speed of disturbance propagation, and shifts in the frequency spectrum. The results reveal that both GPS-TEC and GLONASS-TEC exhibit noticeable disturbances during the specified timeframe. These disturbances are accompanied by the occurrence of "N"-type anomalies in TEC. Notably, at the occurrence of the disturbance, the elevation angle of GPS PRN32 and GLONASS PRN1 satellites is approximately 50°-55°, and their respective distances from the typhoon eye are roughly 350 km and 150 km. The propagation velocity and center frequency of the ionospheric disturbances are located in the range of gravity waves. Specifically, the disturbances propagation speeds of GPS PRN32 and GLONASS PRN1 are approximately 129.36 m/s and 128.33 m/s, respectively, while the center frequencies are about 1.17 mHz and 1.43 mHz. The ionospheric perturbations observed by GPS and GLONASS exhibit certain similarities, which provide valuable insights into the relationship between typhoons and ionospheric disturbances.

Keywords: Typhoon; GPS; GLONASS; TEC; Ionospheric disturbances

1. Introduction

Typhoon is a tropical cyclone, a powerful and profound tropical weather system. The transit of typhoons often brings disastrous weather, such as strong winds, thunderstorms, and floods, which severely impact transportation, communications, electricity, etc., causing people's lives and colossal property damage. A number of studies have shown that typhoon and other severe meteorological activities also have significant effects on the morphology of ionospheric disturbances (Rice et al., 2012; Isaev et al., 2010). For example, characteristics of ionospheric disturbances caused by typhoons and the coupling mechanism were reported (Shen, 1982). Bauer (1958) first discovered the typhoon effect on ionospheric conditions and found that the critical frequency of the F2 layer (foF2) increased, and the surface pressure decreased as the typhoon

* Corresponding author.
E-mail address: sgjin@shao.ac.cn (S. Jin).

https://doi.org/10.1016/j.asr.2024.03.060
0273-1177/

approached the station. Hins (1960) proposed that meteorological activities in the middle and lower atmospheres affect the ionosphere through acoustic gravity waves. However, most traditional studies used ionosonde, Doppler sounders, and other observation instruments to study the coupling relationship between typhoons and the ionosphere (Huang et al., 1985; Xiao et al., 2007), these data were still less or low resolution.

With the continuous development of Global Navigation Satellite System (GNSS), GNSS TEC can study the relationship and coupling between typhoons and ionospheric disturbances (Jin et al., 2014). Xu et al. (2018) used ionospheric TEC data extracted from GPS and GIM observation to study the ionospheric TEC disturbance characteristics before and after typhoon landing, speculating that TEC anomalies were caused by the propagation of acoustic gravity waves caused by typhoons to the ionospheric height. Positive anomalies were detected during Typhoon Hagupit via ionospheric parameter extracted from GPS (Wu et al., 2021). Chou et al. (2017) observed concentric traveling ionospheric disturbances caused by gravity waves generated by Typhoon Meranti through GNSS networks. Based on TEC, Yuan et al. (2019) also used the parameter of electron density data to analyze the ionospheric changes during Typhoon Nepartak, proving that the negative anomalies of the ionosphere during the typhoon were related to the atmosphere–ionosphere coupling effect caused by Typhoon Nepartak from multiple angles. Zhao et al. (2020) simulated Typhoon Meranti and obtained the evolution of the ionospheric disturbance caused by the typhoon, which corresponded well with actual observations. Fu and Jin (2022) discussed the relationship and mechanism of typhoon-induced disturbances during typhoons by using GPS-derived TEC data and found that the higher the intensity of the typhoon is, the greater the magnitude of the ionospheric disturbance is.

Although a large number of studies have shown that typhoons can generate upward propagating acoustic gravity waves and cause ionospheric disturbances, the coupling relationship between typhoons and the ionosphere is very complex. For example, it may be difficult to cause significant changes in TEC when the typhoon intensity is weak (Perevalova et al., 2014). TEC may not change significantly when the distance between SIP and typhoon eye exceeded a certain threshold range. The difference of atmospheric physical environment when typhoon causes ionospheric disturbances may lead to longer or shorter duration of ionospheric disturbance, etc. Therefore, it is still necessary to analyze possible patterns based on a large number of statistical typhoon events (Wen and Jin, 2020). Furthermore, sometimes, GPS data are still limited during the Typhoons, while GLONASS can increase more satellite observations and help study ionospheric disturbances caused by typhoons, which can capture ionospheric disturbance characteristics in a more detailed and comprehensive way.

In this paper, GPS and GLONASS TEC data are jointly used to analyze the ionospheric disturbance changes, disturbance velocity and spectrum changes during 10:00–12:00 UT of Typhoon No. 2114 Chanthu on September 12, 2021 as well as the disturbance rules of the TEC, which will help to characterize further the coupling relationship between the typhoon and the ionosphere. Section 2 describes the data and methods, results and analysis are presented in Section 3, some discussions are shown in Section 4, and finally conclusions is given in Section 5.

2. Data and methods

2.1. Typhoon information

Typhoon Chanthu was the second tropical cyclone rated as a super typhoon by the Joint Typhoon Warning Center in 2021, and its passage brought significant wind and rain to the northern Philippines, China, and Japan. The detailed Typhoon information was shown at https://typhoon.nmc.cn/web.html. As shown in Table 1, typhoon Chanthu formed in the Northwest Pacific Ocean at 8:00 on September 7, 2021, and strengthened into a tropical storm at 17:00 on the same day. At 5:00 on September 8, 2021, typhoon Chanthu intensified into a super typhoon, with a maximum wind speed of level 17 (58 m/s) near the center. As the typhoon continued to strengthen, the maximum wind speed near the center reached 68 m/s at 17:00 on September 10, 2021, and then the typhoon Chanthu weakened slightly, and the maximum wind speed near the center dropped to level 16. On September 14, 2021, Chanthu weakened from a moderate typhoon level to a typhoon level. On September 15, 2021, Chanthu continued to move slowly in the northern part of the East China Sea. At around 19:00 local time on September 17, 2021, typhoon Chanthu landed near Fukutsu City, Fukuoka Prefecture, Japan. Then it gradually degenerated into an extratropical cyclone at 8:00 on September 18, 2021 . Table 1 shows the occurrence and development process of the typhoon, and Fig. 1 shows the track map of the typhoon Chanthu from September 8 to 17, 2021 and the distribution of the GNSS stations.

2.2. Data

In this study, ionospheric TEC is extracted from GPS and GLONASS observation data, which were used to analyze the characteristics of ionospheric disturbances caused by typhoon Chanthu on September 8–17, 2021. The data used were collected from dense and continuous multi-system GNSS network stations in Taiwan with a sampling interval of 30 s and 122 stations in total. The red plus sign in Fig. 1 represents the GNSS stations in Taiwan used in this research. The typhoon information came from the Typhoon Network of the Central Meteorological Observatory, and the selected typhoon Chanthu was the second tropical cyclone given the super typhoon level by the Joint

Table 1
The occurrence and development of Typhoon Chanthu.

Time	Typhoon Center Position	Typhoon Category	Maximum Wind speed (m/s)	Central Pressure (hpa)	Moving direction
2021-9-7 8:00	136.7°, 15.6°	tropical storm	28	982	northwest
2021-9-8 5:00	133°, 16.1°	super typhoon	58	925	west
2021-9-12 14:00	122.3°, 25.2°	strong typhoon	50	935	north
2021-9-14 2:00	123.6°, 31.5°	typhoon	38	965	northeast
2021-9-14 8:00	123.9°, 31.3°	severe tropical storm	30	970	southeast
2021-9-17 8:00	127.5°, 32.9°	tropical storm	23	995	northeast

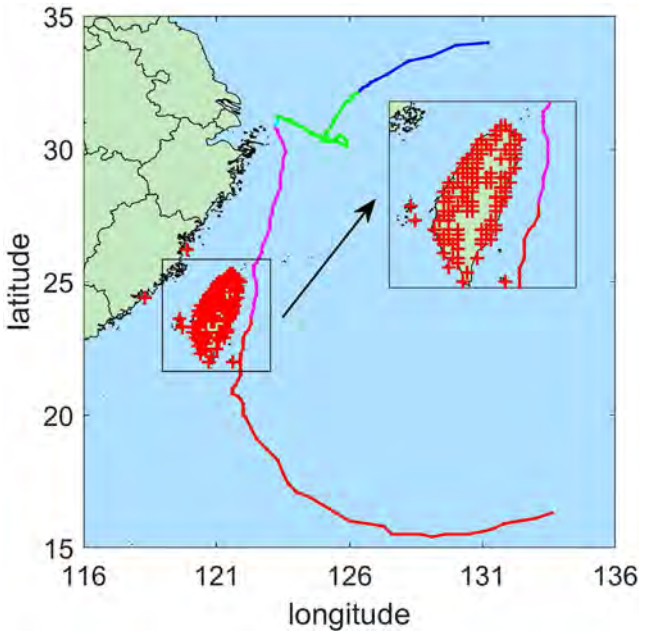

Fig. 1. Track of typhoon Chanthu and GNSS stations distribution, where the red plus sign represents GNSS stations distribution, the line connected by colored dots represents the typhoon track, the red dots represent super typhoon, the magenta dots represent strong typhoon, the blue dots represent typhoon, the green dots represent severe tropical storm, and the blue dots represent tropical storm.

Typhoon Warning Center in 2021. The passing of typhoon Chanthu brought significant wind and rain to the northern Philippines, China, and Japan. Since the ionosphere is affected by solar radiation and geomagnetic disturbances, when analyzing ionospheric anomalies during a typhoon, it is necessary to comprehensively judge whether the space weather is calm during this period. Therefore, F10.7, Dst, and Kp indices are selected to analyze the solar and geomagnetic activity during typhoon Chanthu. The Kp index and F10.7 index were obtained from https://www.gfz-potsdam.de/en/kp-index/, and the Dst index data was obtained from https://wdc.kugi.kyoto-u.ac.jp/wdc/Sec3.html.

2.3. Method

Changes in the ionospheric total electron content (TEC) can broadly reflect ionospheric disturbance. Due to the inherent vertical structure of the Earth's atmosphere and ionosphere, the free electrons are mainly located at the altitude of 200 ~ 400 km. To simplify the ionosphere model, this study assumed that all the free electrons of the whole ionospheric region are concentrated in a thin layer in the F layer, a single-layer model representing all the electron content in the entire ionospheric region. It can approximately represent the vertical TEC content, and the ionospheric height H of 350 km is chosen in this study.

This study uses the dual-frequency GNSS observation data to obtain the ionospheric TEC value (Jin et al., 2017a,b). The RINEX 2.11 was used in this study, and the carrier phase measurements were provided in L1, L2. The carrier phase frequency of the GPS is $f_1 = 1575.42$ MHz, $f_2 = 1227.60$ MHz, and the carrier phase frequency of the GLONASS system is $f_1 = 1602 + k*9/16$ MHz, $f_2 = 1246 + k*7/16$ MHz, where k is 1 to 24, which is the frequency number of each satellite. The same satellite satisfies $L_1/L_2 = 9/7$. Ionospheric TEC can be extracted by the following formula using dual-frequency GNSS observations combined with code phase measurements (Demyanov et al., 2020; Jin et al., 2006 and 2017a,b):

$$STEC = \frac{f_1^2 f_2^2}{40.3\left(f_1^2 - f_2^2\right)}\left(P_1 - P_2 - (d_1 - d_2) + \varepsilon\right) \quad (1)$$

$$STEC = \frac{f_1^2 f_2^2}{40.3\left(f_1^2 - f_2^2\right)}\left(L_1 - L_2 + \lambda_1(N_1 + b_1) - \lambda_2(N_2 + b_2) + \varepsilon\right) \quad (2)$$

where f_1 and f_2 are the carrier phase frequencies of the signal, L is the carrier phase observation value, P is the pseudo-range observation value, λ is the signal wavelength, N is the integer ambiguity resolution, b is the instrumental deviation of the carrier phase, d is the instrument error of the pseudo-range, and ε is the residual error.

The mapping function is used to convert the obtained slant TEC into vertical TEC:

$$vTEC = STEC * cos\left[arcsin\left(\frac{Rsin(z)}{R+H}\right)\right] \quad (3)$$

where R is the radius of the Earth, H is the height of the ionospheric thin shell, and z is the elevation angle. In the TEC calculation, the ambiguity, differential code biases, and other noises are estimated to be constant, and the constant terms can be eliminated by low-frequency filtering to obtain more accurate TEC (Jin et al., 2017; Jin, 2018).

After obtaining the VTEC time series, in order to extract prominent ionospheric disturbances, a fourth-order Butterworth filter is used to remove the effects of ionospheric

puncture point (SIP) motion and ionospheric background changes (Jin, 2018), with a cutoff frequency of 1–3 mHz. This filter is also called a maximum flat filter. The frequency response curve in the pass band is flat to the maximum without ripples, while it gradually drops to zero in the stop band. The higher the order is, the faster the amplitude attenuation in the stop band is. The formula for the Butterworth filter is expressed as follows:

$$|H(\omega)|^2 = \frac{1}{1+(\frac{\omega}{\omega_c})^{2n}} = \frac{1}{1+e^2(\frac{\omega}{\omega_p})^{2n}} \# \quad (4)$$

where n represents the order of the Butterworth bandpass filter, ω_p represents the edge frequency of the pass band, ω_c represents the cutoff frequency, $\frac{1}{1+e^2}$ represents $|H(\omega)|^2$ in the pass band marginal value.

The interquartile range (IQR) has been widely used to detected the characteristics of the ionospheric variations during extreme space weather (Li et al., 2016; Tang et al., 2022). In order to detect the disturbance of the VTEC sequence more effectively, the IQR is used to determine the upper and lower limits of VTEC disturbances when analyzing the anomaly of the filtered VTEC time series. This method does not have any requirements for data distribution and can be applied to various types of data sets. The criteria for judging outliers are mainly based on quartiles and interquartile ranges. Specifically, the VTEC values of the period are arranged in ascending order, and the data set is divided into four parts by three quartiles. These three quartiles are, respectively, the upper quartile Q1, expressing in the VTEC values below this value, which account for 25 % of the total; the median Q2, indicating that the VTEC values below this value account for 50 % of the total; and the lower quartile Q3, indicating that 75 % of the total number of VTEC values are below this value, and then there is:

$$\begin{cases} IQR = Q_3 - Q_1 \\ UP = Q_3 + 1.5 * IQR \ \# \\ LOW = Q_1 - 1.5 * IQR \end{cases} \quad (5)$$

where IQR represents the interquartile range, $'UP'$ and $'LOW'$ represent the upper and lower limits of the value, respectively. Consequently, an abnormal value is one that is less than $Q_1 - 1.5 * IQR$ or greater than $Q_3 + 1.5 * IQR$. The VTEC value greater than the upper limit is considered a positive anomaly, while an observed value less than the lower limit is classified as a negative anomaly.

3. Results and analysis

3.1. Solar-terrestrial environment during typhoons

Solar and geomagnetic activities are the primary factors affecting the ionospheric TEC changes (Zhang et al., 2012). Therefore, before analyzing and studying the ionospheric disturbance caused by typhoon Chanthu, the geomagnetic and solar activity levels during the impact of Chanthu should be analyzed. Fig. 2 shows the changes in the geomagnetic activity index Kp, Dst, and solar activity index F10.7. From September 3, 2021 to September 23, 2021, it can be seen from Fig. 2 that during the typhoon Chanthu, the Kp index of geomagnetic activity was less than or equal to 4 nT, and the Dst index was at a low level (-20 nT $\sim$ 20 nT). F10.7 gradually decreased and tended to be stable after the typhoon, and the solar activity index F10.7 was below 100 sfu (Kong et al., 2022; Ke et al., 2019). Therefore, during the Typhoon Chanthu period, the geomagnetic activities were mainly quiet, and the solar activities were low. During this period, geomagnetic and solar activities cannot cause ionospheric disturbances, so the influence of geomagnetic and solar activities can be ignored.

3.2. Air pressure changes

In order to study the relationship between changes in air pressure and changes in the ionosphere, the air pressure data obtained from Meteomanz.com every 3 h from September 1 to September 31, 2021, were used to analyze air pressure changes during this typhoon, as shown in Fig. 3(b). Fig. 3(a) shows the location distribution of the three selected stations, TAIBEI, TAIZHONG and TAINAN. It can be seen that the selected stations are close to the GNSS network stations. In Fig. 3(b), the black solid line represents TAIBEI station, the red dotted line represents TAIZHONG station, and the blue dotted line represents TAINAN station. It can be seen from Fig. 3(b) that since 12:00 UT on September 10, 2021, the air pressure has dropped rapidly. At this time, Chanthu was in the super typhoon stage, advancing from southeast to northwest, and the typhoon track was close to Taiwan Province. The air pressure reached the lowest value of about 995 Hpa in the early morning of the 12th, and then the air pressure rose rapidly and gradually stabilized on the 14th September 2021.

3.3. Ionospheric disturbance from GPS-TEC

The typhoon track during the selected time of this study is close to Taiwan Province, and the stations are densely distributed. Fig. 4(a) is the SIP tracks of station LIU2 at 10:00–12:00 UT. The black five-pointed star represents the typhoon eye position, the red triangle indicates the position of the stations, and the blue curve indicates the SIP trajectory of each satellite that station LIU2 observes during this period. It can be seen from Fig. 4(a) that during the period from 10:00 to 12:00 UT, there are a large number of visible satellites. Here PRN32 was taken as an example to study the changes of GPS-TEC. The red dotted line in Fig. 4(b) represents the SIP tracks of each station for PRN32. It can be seen that the track of PRN32 moves from northwest to southeast, and most of them are located in the north of the typhoon eye and are relatively close to the stations. The magenta asterisk indicates typhoon activity at that time.

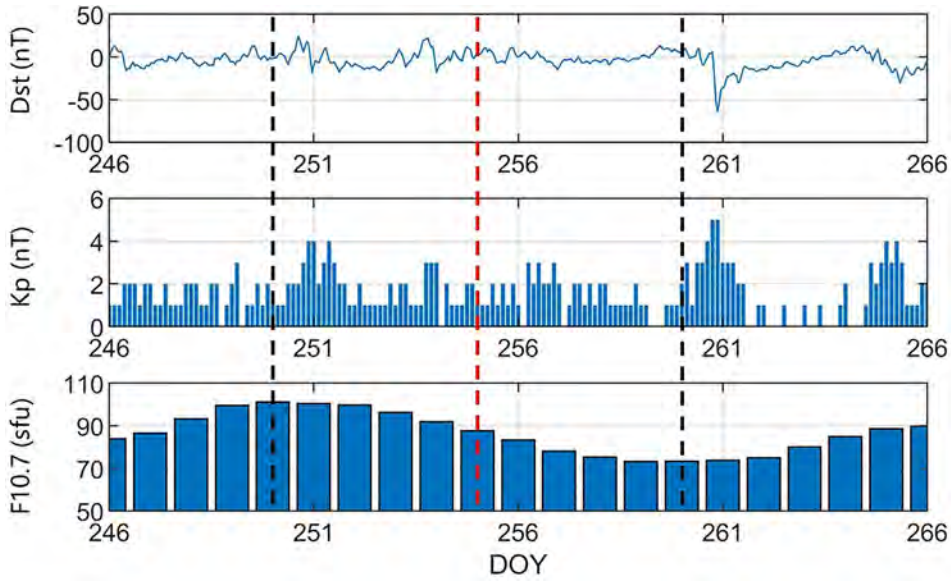

Fig. 2. The F10.7, Kp, and Dst indices from DOY 246 to DOY 266. The black dotted line indicates the time when typhoon arises and disappears, and the red dotted line indicates the studied period in this study.

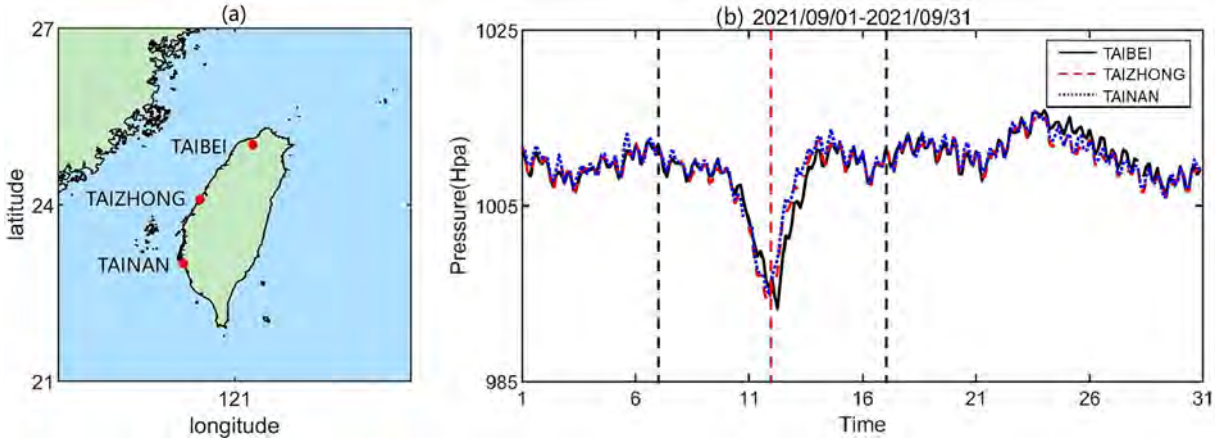

Fig. 3. Distribution of TAIBEI, TAIZHONG, and TAINAN stations (a), and time series of pressure changes at selected three stations (b). The black dotted line indicates the time when typhoon arises and disappears, and the red dotted line indicates the studied period in this study.

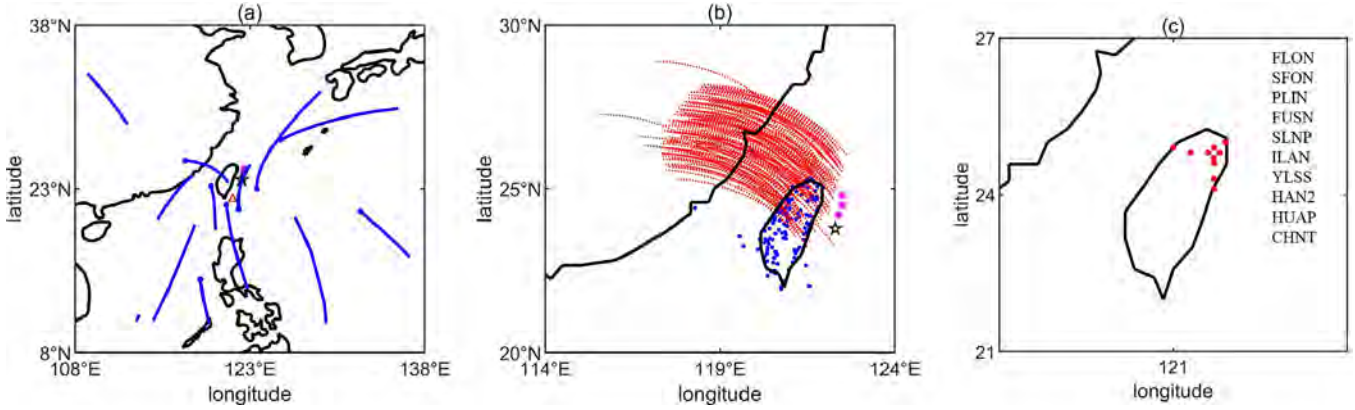

Fig. 4. SIP tracks of each satellite at station LIU2 (a), SIP tracks of satellite PRN32 (b) and the location distribution of selected stations (c) during 10:00–12:00 UT, 12 September 2021.

The filtered VTEC time series of PRN32 during 10:00–12:00 UT was used to analyze the disturbance's waveform and the disturbance's variation rules. Fig. 5 shows the time series of the filtered VTEC of the PRN32 at 10:00–12:00 UT. The location distribution of some stations with significant VTEC changes at this time was shown in Fig. 4(c), and the station names in the legend on the right are ordered by decreasing latitude. It can be seen from Fig. 5 that most of them show "N" type anomalies, with prominent disturbances at each station and concentrated disturbances at 11:00 UT, among which the disturbance amplitudes of CHNT, FLON, FUSN, and HUAP all reached 0.19 TECU. Station HAN2, HUAP, ILAN, PLIN, SLNP, and YLSS showed positive "N" type anomalies, which was a positive anomaly appeared first, followed by a negative anomaly, and then the disturbance amplitude decreased and became stable. Station FLON, FUSN, and SFON showed inverted "N" type anomalies. In these stations, negative anomalies first appeared, then positive anomalies appeared, and the positive and negative ones were apparent. In the VTEC time series of the selected stations in Fig. 5, the maximum abnormal value reaches 0.19 TECU, and the minimum abnormal value is 0.14 TECU. During the selected time, the anomaly appeared in the northwest of the typhoon eye, and the filtered VTEC showed the same variation trend with certain regularity. The VTEC disturbance phenomenon is even more apparent during 10:40–11:10 UT.

Since the geometric structure of the observation satellites at each station is the same, the number of satellites that can be observed at all stations is similar. Each observation ray has a sub-satellite point to form a regular area. The two-dimensional disturbance map can be used to analyze the ionospheric disturbance caused by typhoons (Li et al., 2016). Fig. 6 shows the distribution of SIP of satellites observed from GPS-TEC at 10:51, 10:57, 11:04, and 11:10 UT. The shape of the distribution map of all sub-satellite points obtained from the observation of different satellites by each station in each subfigure is similar to that of Taiwan Province, in which the pentagram represents the position of the typhoon eye, and the color bar indicates the range of the VTEC changes. The range from blue to red represents the range from −0.2 TECU to 0.2 TECU. According to the change in the two-dimensional disturbance map at each time, the variation of the ionospheric disturbance can be seen, and the distribution of the ionosphere disturbance can be analyzed. It can be seen that the disturbance of satellite PRN32 in the subfigure (a) changes significantly, and there are apparent positive and negative anomalies at the selected time points. The anom-

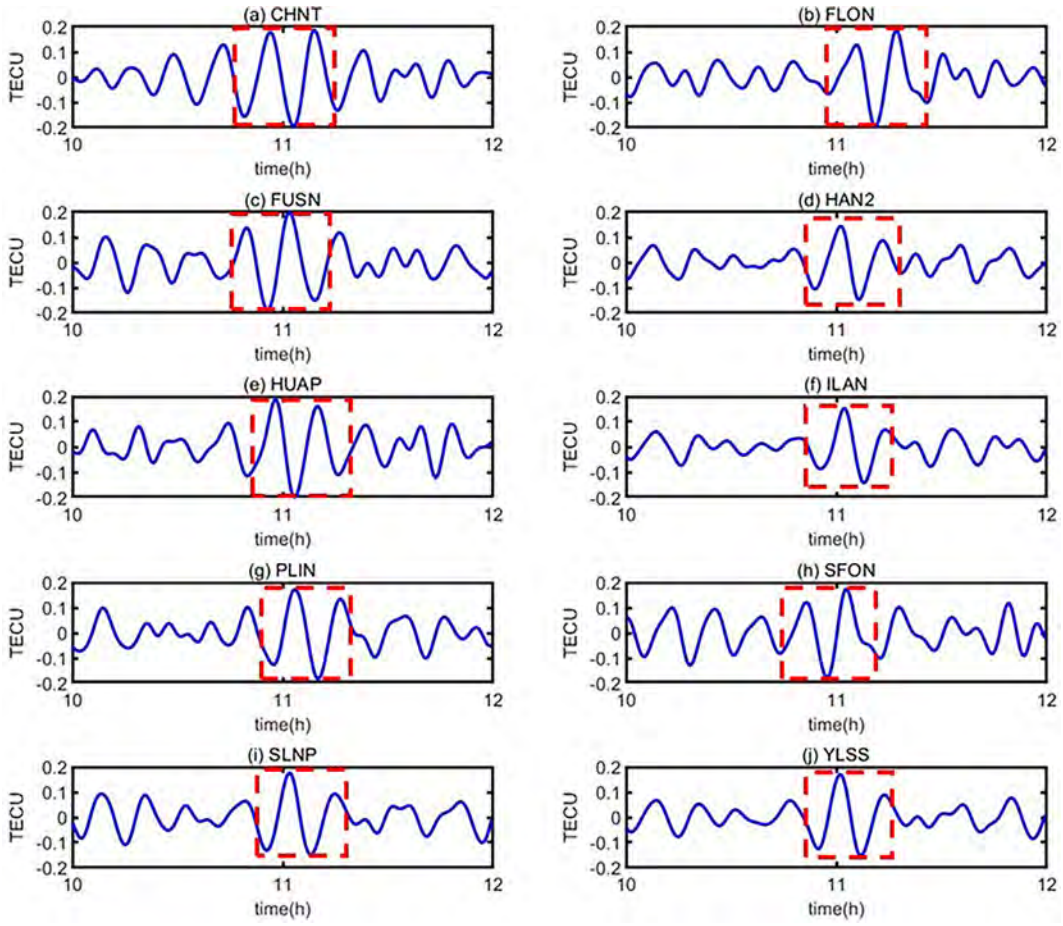

Fig. 5. Filtered VTEC time series of PRN32 at selected stations during 10:00–12:00 UT, 12 September 2021.

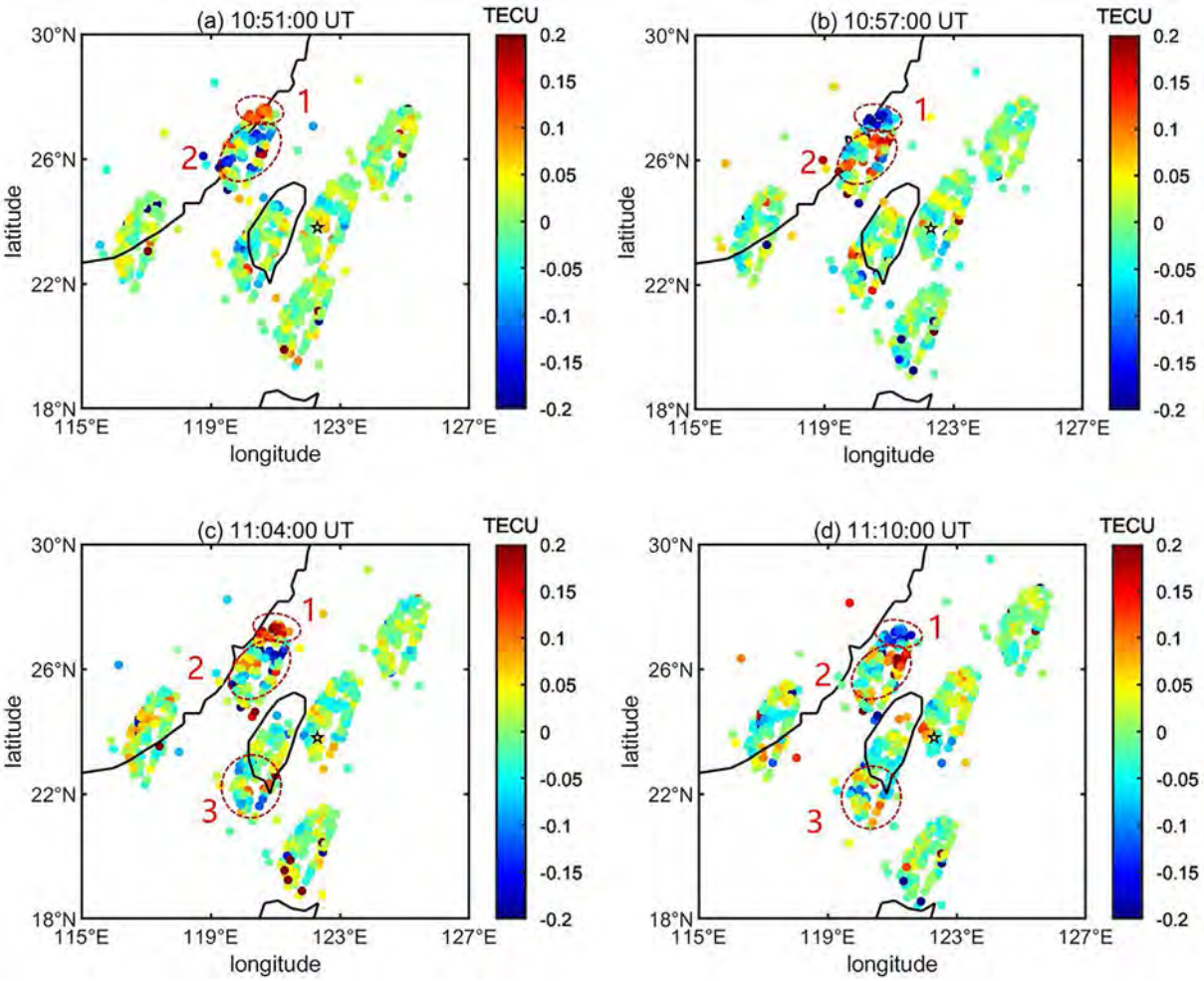

Fig. 6. Spatial and temporal variation of the ionospheric disturbances of GPS-TEC at 10:36–10:51 UT on September 12, 2021. The color bar represents the amplitude of TEC changes, and the colored solid circle points show the position of SIP.

aly range of zone "1" experienced two disturbances from positive anomalies to negative anomalies during 10:51–11:10 UT, with positive and negative anomalies reaching 0.19 TECU, and the abnormality range of zone "2" also has two disturbances from negative abnormality to positive abnormality. In addition, in Fig. 6(c) and Fig. 6(d), the satellite PRN10 detected a weaker ionospheric disturbance phenomenon. The observed disturbances were distributed in the western direction of the typhoon center, and no significant disturbances were observed in the east of the typhoon eye.

3.4. Ionospheric disturbance from GLONASS-TEC

The ionospheric disturbances are further extracted from GLONASS observation data in Taiwan on September 12, 2021 with 122 stations. The ionospheric VTEC value is calculated through the dual-frequency observation method. As shown in Fig. 7(a), the SIP trajectory of PRN1 is given, and the selected time range is 10:00–12:00 UT. According to the trajectory of the SIP, the satellite's trajectory moves from northwest to southeast, and most of them are located east of the typhoon eye, which is closer to the station.

The filtered VTEC time series values of the PRN1 satellite are analyzed from GLONASS. Fig. 8 shows the VTEC changes at some stations from 10:00–12:00 UT on September 12, 2021. The location distribution of some stations with significant VTEC changes at this time was shown in Fig. 7(b), and the station names in the legend on the right are sorted by decreasing latitude. It can be seen from Fig. 8 that although the disturbance phenomenon at each station is different, there is a certain regularity in the disturbance. Anomalies mainly appeared between 10:50–11:10 UT. Before 10:50 UT, the filtered VTEC was relatively quiet, with only slight fluctuations. From 10:40 UT, most stations appeared to have apparent ionospheric anomalies, and the disturbance lasted for several minutes, mainly concentrated between 10:50–11:10 UT. The station STA1 had a maximum anomaly of 0.17 TECU during this period. After 11:10 UT, the fluctuation amplitude of TECU at each station decreased, and until no obvious abnormality occurred.

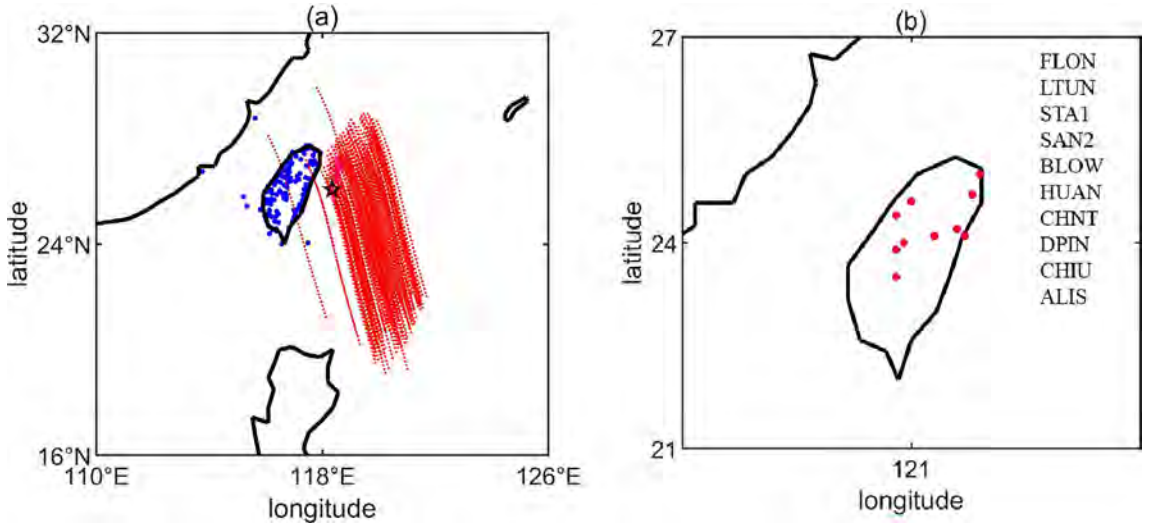

Fig. 7. SIP trajectory of GLONASS PRN1 during 10:00–12:00 UT, 12 September 2021 (a) and the location distribution of selected stations (b).

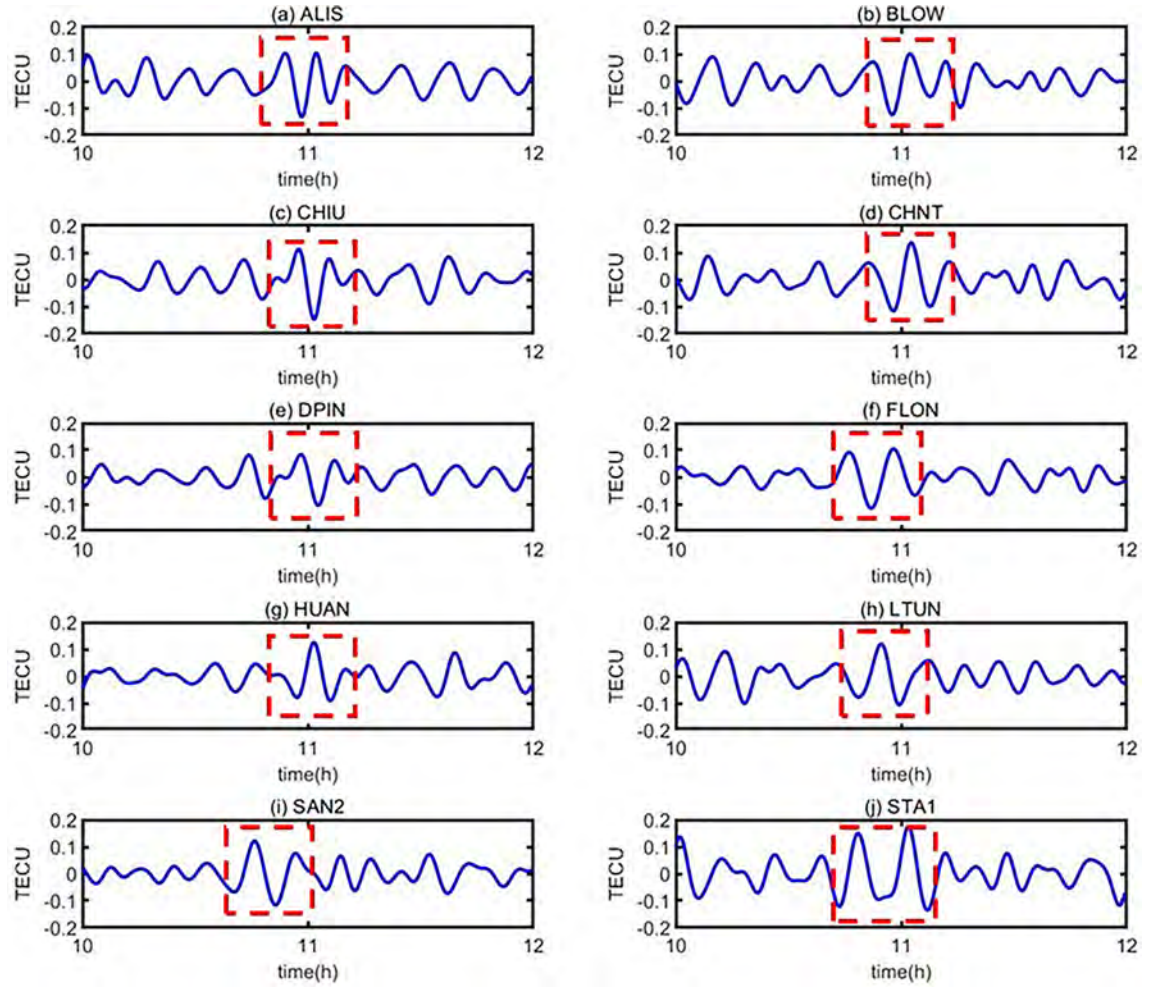

Fig. 8. Filtered VTEC time series of PRN1 at selected stations during 10:00–12:00 UT, 12 September 2021.

In the VTEC time series of the PRN1 satellite given in Fig. 8, it can be seen that most of them present "N" type anomalies, that is, positive anomalies appeared first, then negative anomalies, and finally positive anomalies, among which the fluctuation patterns of the stations CHNT, HUAN, LTUN, and SAN2 are similar. At the same time, the anomalies of the station DPIN are slightly weaker, with the maximum anomaly value of only 0.10 TECU.

In order to see the spatiotemporal changes of ionospheric anomalies more clearly, Fig. 9 shows the two-dimensional ionospheric disturbances over Taiwan Province during part of the period from 10:00 to 12:00 UT on September 12, 2021. The black curve represents the plate curve, and the abnormal change trend of the ionosphere can be found through the changes of TEC at different times. In the two-dimensional disturbance diagram of the ionosphere at four times of 10:52, 10:57, 11:02, and 11:10 UT shown in Fig. 9, the PRN1 satellite has prominent disturbances, and the main anomalies appear in the southeast direction relative to the eye of the typhoon. At 10:52 UT, there were apparent positive and negative anomalies in the ionosphere, in which the positive anomalies appeared in the northeast relative to the eye of the typhoon. Meanwhile, the negative anomalies mainly appeared in the south of the eye of the typhoon. Five minutes later, at 10:57 UT, there was an apparent negative anomaly, with the anomaly value of 0.1495 TECU. At 11:02 UT, the ionospheric anomaly was still noticeable, with an obvious positive anomaly. At 11:10 UT, the positive anomaly weakened, and the negative anomaly in the southern part of the typhoon eye was relatively apparent.

3.5. Comparative analysis of GPS-TEC and GLONASS-TEC disturbances

In order to explore the changes in satellite elevation angle and the distance between SIP and typhoon eye, Fig. 10 shows the relationship between the altitude angle and the distance between SIP and the typhoon eye observed by GPS PRN32 and GLONASS PRN1 satellites at selected stations during 10:00–12:00 UT. Fig. 10(a-e) shows the results of the data from GPS PRN32 stations, and the blue solid line in the figure represents the change in the satellite elevation angle during this period. It can be seen that the elevation angle of the GPS PRN32 satellite varies in the range of 30° – 90°, and the elevation angle at the moment of the disturbance occurance is about 55°. The red solid line in the figure represents the change in the distance between SIP and the eye of the typhoon during this period. It is clear that during this period, the distance between SIP and the eye of the typhoon eye was less than 600 km, and the distance was about 350 km when the disturbance occurred. It can be seen from the GLONASS PRN1 stations results in Fig. 10(f-j) that during this period, the elevation angle of the GLONASS PRN1

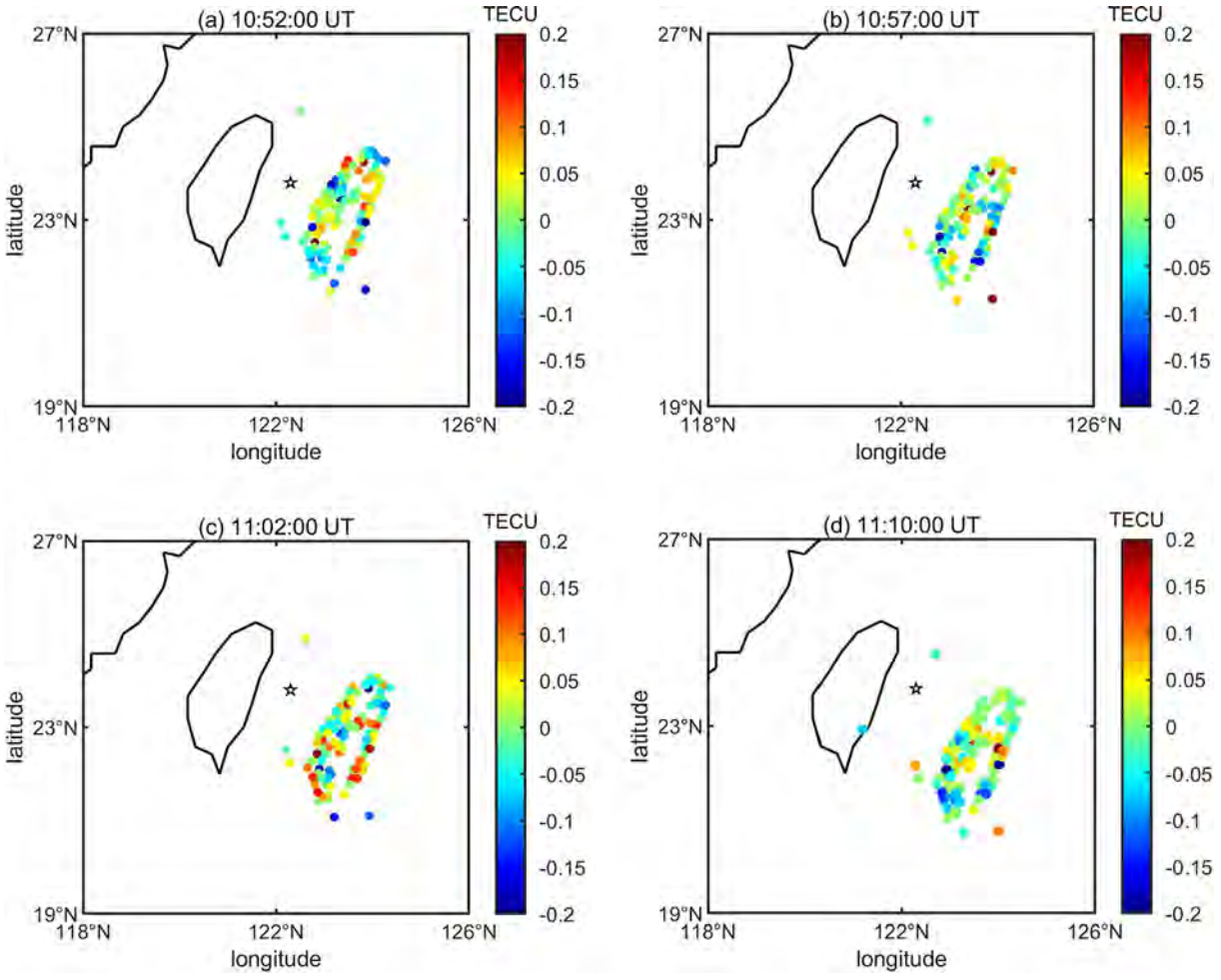

Fig. 9. Temporal and spatial variations of GLONASS-TEC ionospheric disturbances at 10:52, 10:57, 11:02, and 11:10 UT on September 12, 2021. The color bar represents the amplitude of TEC changes, and the colored solid circle points show the position of SIP.

is in the range of 20°-60°, and the elevation angle at the time of the ionospheric disturbance is about 50°. The SIP and typhoon eye distances are all less than 600 km, and the distance is about 120 km when the disturbance occurs. It can be concluded that when significant disturbances occur in the ionosphere, the elevation angle range is 50°-55°, and at the time when the disturbance occurs, the distance between the SIP and the typhoon eye observed by each GPS satellite station is greater than that of the GLONASS satellite.

Through the analysis of GPS-TEC and GLONASS-TEC time series diagrams and two-dimensional disturbance diagrams, it can be seen that there are obvious disturbance phenomena in the ionosphere during the selected time. In order to further explore, a time-distance diagram is used to analyze the disturbance type. Fig. 11 shows the linear relationship between the VTEC value extracted by the Butterworth filtering method and the distance between the SIP of the satellite and the typhoon eye over time. Linear fitting is performed at the position with the largest value for the disturbed VTEC during 10:00–12:00UT on September 12, 2021, and the approximate propagation speed of the two disturbances is estimated. It can be observed that the ionospheric disturbance propagation velocity of GPS PRN32 is about 129.36 m/s, and that of the GLONASS PRN1 disturbance is about 128.33 m/s. The two fitting velocities are similar and within the range of gravity waves.

In order to further analyze the characteristics of the ionospheric disturbance caused by typhoon Chanthu, the frequency domain of the disturbance signal was further analyzed. Welch method was used for power spectrum analysis to divide the signal into multiple overlapping segments, perform Fourier transform on each segment, and average the results to obtain power spectral density estimation. According to this method, the disturbance signal was transformed from the time domain to the frequency domain to analyze the spectrum change of VTEC, observe the distribution of the disturbance signal power in the frequency domain, analyze the signal spectrum distribution, and understand the relative loudness of different frequency components in the signal to understand the spectral characteristics of the typhoon better. Fig. 12 shows the power spectral density diagram (PSD) of GPS PRN32 and GLONASS PRN1 satellite VTEC variations at CHNT, FLON, and other stations, where the x-axis is the frequency, and the y-axis represents the VTEC variations power with frequency. Here, the logarithmic scale represents the power, and 10*log10 was used to convert the power to decibel (dB) units. As it can be seen from Fig. 12, the center frequencies of GPS PRN32 and GLONASS PRN1 are 1.17 mHz and 1.43 mHz, respectively, and the center frequency ranges are similar, which are both within the frequency range of gravity waves, indicating that Typhoon Chanthu excited gravity waves and caused the occurrence of ionospheric disturbances.

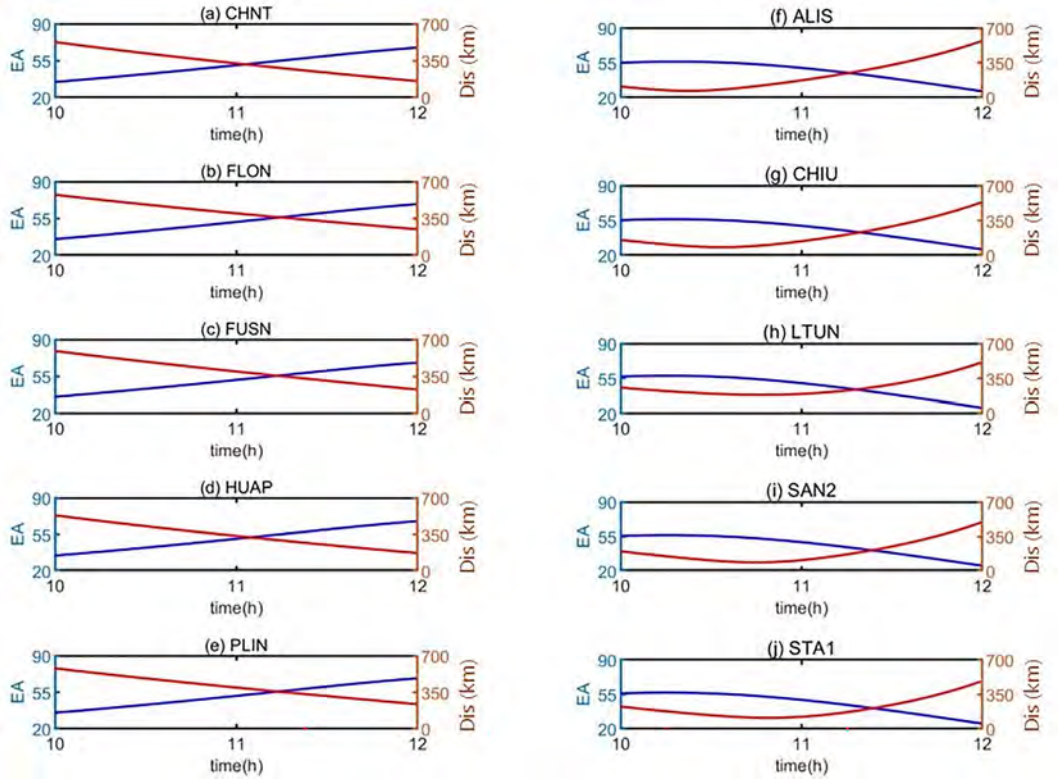

Fig. 10. Elevation angle variations in the blue line and the distance between SIP and typhoon eye in the red line for GPS PRN32 (a-e) and GLONASS PRN1 (f-j) at selection stations during 10:00–12:00 UT, 12 September 2021.

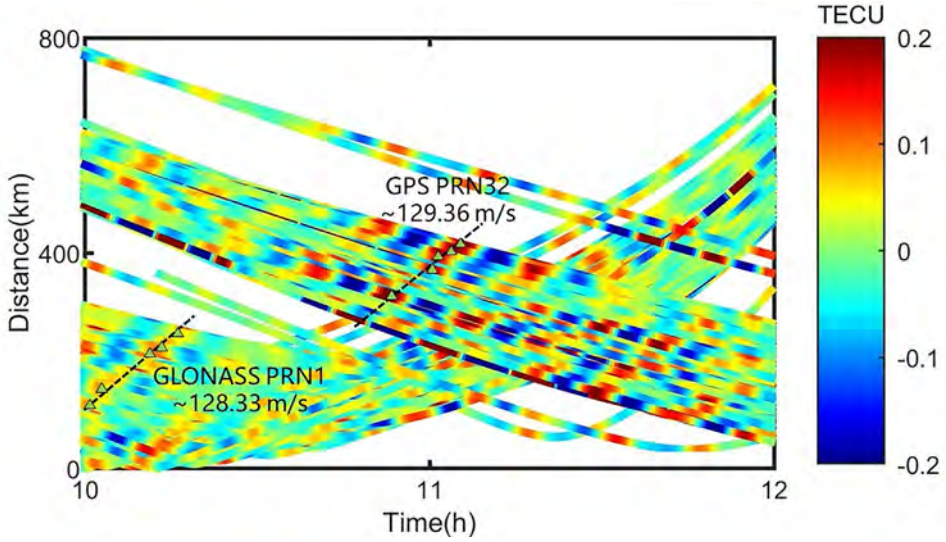

Fig. 11. GPS PRN32 and GLONASS PRN1 velocity fitting results during 10:00–12:00 UT, 12 September 2021.

4. Discussion

From the above study, it can be seen that during 10:00–12:00 UT on September 12, 2021, gravity waves excited by Typhoon Chanthu caused ionospheric disturbances. The relationship between air pressure changes and ionospheric disturbances was studied, and it was found that the air pressure on September 11–12, 2021 was significantly lower than that at other times, and the sudden drop in air pressure at this time was mostly related to the proximity of the typhoon track to the meteorological station (Bauer., et al. 1958). As shown in Fig. 3, the air pressure showed an obvious downward trend since 12:00 UT on September 10. When Typhoon Chanthu was in the super typhoon with the center of the typhoon at 17.4°N, 123.7°E, its trajectory changed from northwest to north and gradually approached Taiwan. On the early morning of September 12, the air pressure reached its lowest level, and then quickly recovered. After September 13, the air pressure fluctuation was relatively stable, and the typhoon track continued to move away from Taiwan. This result was consistent with the findings of Bauer (1958) that as the

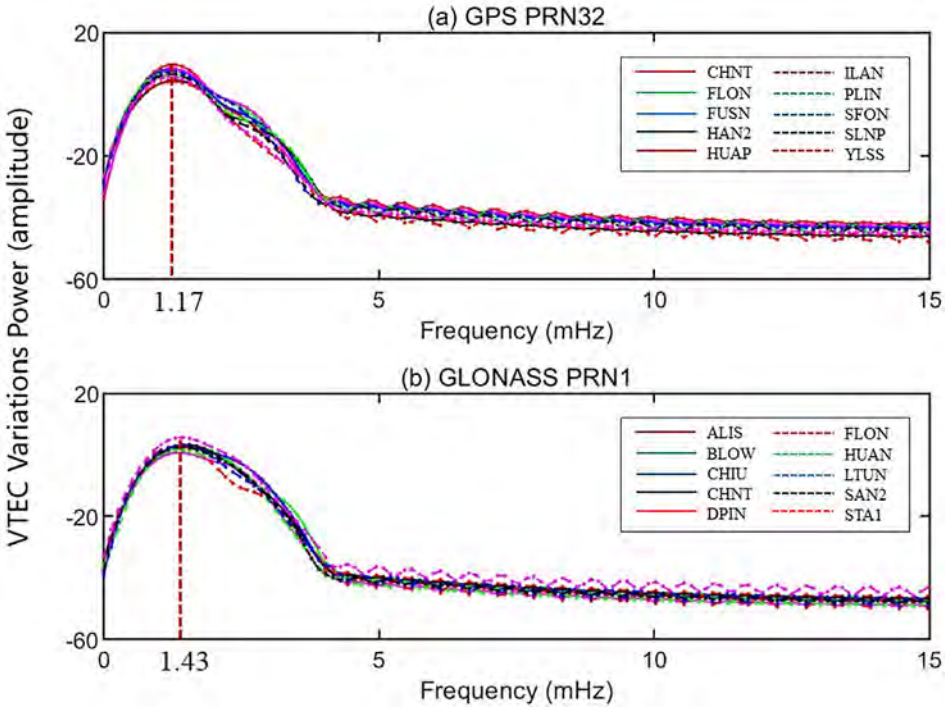

Fig. 12. VTEC variations power with frequency.

typhoon approached the station, the surface air pressure decreased and reached the minimum value when it was closest to the station.

In this study, GPS data were used to study the characteristics of ionospheric disturbances caused by typhoon Chanthu, while GLONASS data was also used to increase the number of observation satellites and improved the reliability of the results. From the analysis of the Butterworth-filtered VTEC time series, it was found that the ionospheric disturbances observed by GPS PRN32 and GLONASS PRN1 in this study were concentrated at about 11:00 UT, and show an "N"-type anomaly, which indicated the feasibility and effectiveness of monitoring ionospheric disturbances by two GNSS systems. In addition, the gravity waves excited by typhoon propagated in the middle and lower atmosphere in the form of concentric rings, and the TEC perturbations at the SIP of GPS and GLONASS satellites at different times showed that the source of the ionospheric disturbances caused by Typhoon Chanthu was located near the typhoon eye. At this time, the typhoon passed through the eastern region of Taiwan and was relatively close to Taiwan.

The results of this study indicated that the ionospheric disturbances may be larger when the distance between the SIP and the typhoon eye is longer. For example, the GPS PRN32 perturbation amplitude was larger than that of GLONASS PRN1. Moreover, as shown in Fig. 10, when the ionospheric disturbance occurred, the distance between the SIP of GPS PRN32 and the typhoon eye was farther than that of GLONASS PRN1. Therefore, it may have a certain correlation between the disturbance amplitude and the distance.

Finally, the occurrence of typhoons affects the ionospheric state. Although this study has analyzed some characteristics of the ionospheric disturbances caused by gravity waves excited by Typhoon Chanthu, more detailed studies on ionospheric disturbance process and coupling are still needed to explore the relationship between typhoons and ionospheric disturbances with more cases in the future. Furthermore, ionospheric disturbances are affected by many factors, which should be seperated. Although the results of the same satellite for different stations at the same time have certain regularities, there are also a little differences. Further detailed study is needed to discuss the relationship between typhoons and ionospheric disturbances with denser GNSS observations and more typhoon events in the future.

5. Conclusions

This study analyzed the ionospheric disturbances caused by typhoon Chanthu using GPS and GLONASS data extracted from GNSS observations in Taiwan. After excluding the influence of solar activity and geomagnetic activity, the ionospheric disturbances characteristics of the PRN32 and the PRN1 following the Typhoon Chanthu during 10:00–12:00 UT on September 12, 2021 were estimated and analyzed from GPS and GLONASS data:

(1) After the upper and lower limits were determined based on the interquartile range method, apparent ionospheric disturbance phenomena were observed during the Typhoon Chanthu, accompanied by the appearance of positive and negative anomalies. Most of them showed "N" type anomalies.
(2) The elevation angle of the GPS PRN32 and GLONASS PRN1 satellites was about 50°-55° when the disturbance occurred. The distance between SIP and the typhoon eye is within 600 km. The distance between the SIPs of GPS satellites and the eye of the typhoon was about 350 km, and the distance between the SIPs of GLONASS satellites and the eye of the typhoon was about 150 km when the significant disturbances occurred.
(3) The disturbance propagation velocities of GPS PRN32 and GLONASS PRN1 were about 129.36 m/s and 128.33 m/s, respectively, which were similar in magnitude and both within the range of gravity waves. Its center frequency was in the range of 0.8–2.1 mHz, and the center frequency of GPS PRN32 was slightly smaller than that of GLONASS PRN1.

CRediT authorship contribution statement

Mengwei Ma: Conceptualization, Data curation, Formal analysis, Investigation, Methodology, Resources, Software, Validation, Visualization, Writing – original draft, Writing – review & editing. **Shuanggen Jin:** Conceptualization, Methodology, Resources, Writing – review & editing. **Xuzhan T. Jin:** Writing – review & editing.

Declaration of competing interest

The authors declare that they have no known competing financial interests or personal relationships that could have appeared to influence the work reported in this paper.

Acknowledgments

This work was supported by National Natural Science Foundation of China (NSFC) Project (Grant No. 12073012) and authors gratefully acknowledged the Taiwan Central Weather Bureau (CWB) for providing the GNSS data.

References

Bauer, S.J., 1958. An apparent ionospheric response to the passage of hurricanes [J]. J. Geophys. Res. 63 (1), 265–269. https://doi.org/10.1029/JZ063i001p00265.

Chou, M.Y., Lin, C.C.H., Yue, J., Tsai, H.F., Sun, Y.Y., Liu, J.Y., Chen, C.H., 2017. Concentric traveling ionosphere disturbances triggered by super typhoon meranti (2016). Geophys. Res. Lett. 44 (3), 1219–1226. https://doi.org/10.1002/2016GL072205.

Demyanov, V.V., Sergeeva, M.A., Fedorov, M.E., Ishina, T.V., Gatica-Acevedo, V.J., Cabral-Cano, E., 2020. Comparison of TEC calcula-

tions based on Trimble. Javad, Leica, and Septentrio GNSS Receiver Data, Remote Sens. 12, 3268. https://doi.org/10.3390/rs12193268.

Fu, J., Jin, S., 2022. Characterization of Ionospheric Disturbances Following Multiple Typhoons Using GPS-Derived TEC. J. Geophys. Res. Space Phys. 128. https://doi.org/10.1029/2022JA030457.

Hins, C.O., 1960. Internal atmospheric gravity waves at ionospheric heights[J]. Can. J. Phys. 38, 1441–1481. https://doi.org/10.1139/p60-150.

Huang, Y.N., Cheng, K., Chen, S.W., 1985. On the detection of acoustic-gravity waves generated by typhoon by use of real time HF doppler frequency shift sounding system[J]. Radio Sci. 20 (4), 897–906. https://doi.org/10.1029/RS020i004p00897.

Isaev, N.V., Kostin, V.M., Belyaev, G.G., et al., 2010. Disturbances of the topside ionosphere caused by typhoons[J]. Geomag. Aeron. 50, 243–255. https://doi.org/10.1134/S001679321002012X.

Jin, S., 2018. Two-mode ionospheric disturbances following the 2005 northern California offshore earthquake from GPS measurements[J]. J. Geophys. Res. Space Phys. 123 (10), 8587–8598. https://doi.org/10.1029/2017JA025001.

Jin, S.G., Jin, R., Kutoglu, H., 2017b. Positive and negative ionospheric responses to the March 2015 geomagnetic storm from BDS observations. J. Geod. 91 (6), 613–626. https://doi.org/10.1007/s00190-016-0988-4.

Jin, S., Park, J., Wang, J., Choi, B., Park, P., 2006. Electron density profiles derived from ground-based GPS observations. J. Navig. 59 (3), 395–401. https://doi.org/10.1017/S0373463306003821.

Jin, S., Jin, R., Li, J.H., 2014. Pattern and evolution of seismo-ionospheric disturbances following the 2011 Tohoku earthquakes from GPS observations[J]. J. Geophys. Res. Space Phys. 119 (9), 7914–7927. https://doi.org/10.1002/2014JA019825.

Jin, S., Jin, R., Li, D., 2017a. GPS detection of ionospheric rayleigh wave and its source following the 2012 haida gwaii earthquake[J]. J. Geophys. Res. Space Phys. 122 (1), 1360–1372. https://doi.org/10.1002/2016JA023727.

Ke, F., Wang, J., Tu, M., et al., 2019. Characteristics and coupling mechanism of GPS ionospheric scintillation responses to the tropical cyclones in Australia. GPS Solutions 23, 1–14. https://doi.org/10.1007/s10291-019-0826-2.

Kong, J., Shan, L., Yan, X., Wang, Y., 2022. Analysis of ionospheric disturbance response to the heavy rain event. Remote Sens. (Basel) 14, 510. https://doi.org/10.3390/rs14030510.

Li, W., Guo, J., Yue, J., Shen, Y., Yang, Y., 2016a. Total electron content anomalies associated with global VEI4+ volcanic eruptions during 2002–2015. J. Volcanol. Geoth. Res. 325, 98–109. https://doi.org/10.1016/j.jvolgeores.2016.06.017.

Li, Z., Tang, L., Zhang, X.H., 2016b. Detection of ionospheric disturbances induced by the 2015 Nepal earthquake using GPS TEC [J]. Geod. Geodyn. 9, 757–760. https://doi.org/10.14075/j.jgg.2016.09.002.

Perevalova, N.P., Sankov, V.A., Astafyeva, E.I., Zhupityaeva, A.S., 2014. Threshold magnitude for Ionospheric TEC response to earthquakes. J. Atmos. Sol. Terr. Phys. 108, 77–90. https://doi.org/10.1016/j.-jastp.2013.12.014, ISSN 1364-6826.

Rice, D.D., Sojka, J.J., Eccles, J.V., et al., 2012. Typhoon Melor and ionospheric weather in the asian sector: a case study[J]. Radio Sci. 47 (04), 1–9. https://doi.org/10.1029/2011RS004917.

Shen, C.S., 1982. The correlations between the typhoon and the foF2 of ionosphere [J]. Chinese Journal of Space Science 2 (4), 335–340. https://doi.org/10.11728/cjss1982.04.335.

Tang, J., Gao, X., Yang, D., Zhong, Z., Huo, X., Wu, X., 2022. Local persistent ionospheric positive responses to the geomagnetic storm in august 2018 using BDS-GEO satellites over low-latitude regions in eastern hemisphere. Remote Sens. (Basel) 14, 2272. https://doi.org/10.3390/rs14092272.

Wen, Y.D., Jin, S.G., 2020. Traveling ionospheric disturbances characteristics during the 2018 typhoon Maria from GPS observations. Remote Sens. 12 (4), 746. https://doi.org/10.3390/rs12040746.

Wu, M.Y., Li, Z.Q., Zhang, R.P, et al. Analysis of abnormal changes of ionospheric TEC in the track of No.2004 Typhoon Hagupit [J]. Journal of Navigation and Positioning, 21,9(3): 104-110. doi: 10.16547/j.cnki.10-1096.20210317.

Xiao, S.G., Zhang, D.H., Xiao, Z., 2007. Study on the detectability of typhoon -generated acoustic-gravity waves [J]. Chinese Journal of Space Science 27 (1), 35–40. https://doi.org/10.11728/cjss2007.01.035.

Xu, J.J., Ke, F.Y., Zhang, X.W., 2018. Study on the characteristics of the ionospheric TEC disturbances caused by typhoon based on ground-based GPS data [J]. Global Positioning Systems 43 (6), 98–104. https://doi.org/10.13442/j.gnss.1008-9268.2018.06.017.

Yuan, J.G., Li, W., Yue, J.P., et al., 2019. An analysis of ionospheric disturbances associated with Nipartak typhoon by GNSS and COSMIC measurements [J]. Science of Surveying and Mapping 44 (03), 63–69. https://doi.org/10.16251/j.cnki.1009-2307.2019.03.011.

Zhang, D.H., Mo, X.H., Ercha, A., et al., 2012. Case study of ionospheric fluctuation over mid-latitude region during one large magnetic storm [J]. Sci. China Technol. Sci. 55 (5), 1198–1206. https://doi.org/10.1007/s11431-012-4785-x.

Zhao, Y.X., Deng, Y., Wang, J.S., et al., 2020. Tropical cyclone-induced gravity wave perturbations in the upper atmosphere: GITM-R simulations [J]. J. Geophys. Res. 125 (7). https://doi.org/10.1029/2019JA027675 e2019JA027675.